

Numerical investigations of retrogressive failure in sensitive clays: revisiting 1994 Sainte-Monique slide, Quebec

Abstract Retrogressive slope failure is ubiquitous in regions of abundant sensitive clays with its mechanism yet to be understood comprehensively. This study gives numerical investigations of retrogressive slope failure with a focus on the 1994 Sainte-Monique slide, Quebec, using a large deformation finite element method. Failure mechanisms and post-failure behaviours including the global kinematics and retrogression distance are highlighted with controlling factors discussed in parametric studies. Key features of post-failure behaviours of the 1994 Sainte-Monique slide are reproduced with the configuration of sliding mass deposits comparable to the site investigations. Post-failure kinematics and retrogression distance are sensitive to sensitivity, brittleness and viscosity of soils and riverbed geometry. Parametric studies may contribute to assess potential retrogression recurrence in the region and its retrogression distance upon current set of in situ parameters.

Keywords Slides · Retrogressive failure · Sensitive clays · Shear band · Large deformation numerical modelling

Introduction

Many natural clays undergo strain softening during shearing, characterised by distinct peak and residual shear strengths and usually termed as sensitive clays. In northern countries, such as Norway and Canada, sensitivity of the so-called quick clays can be as high as over 100 (Crawford 1968; Lundstrom et al. 2009; Quinn et al. 2011; Gylland et al. 2013), and thus, slope failure is ubiquitous in those regions (Skempton 1964, 1985; Kerr and Drew 1968; Gregersen and Loken 1979; Solberg et al. 2008). Loss of shear strength during shearing can cause rapid escalation of the slide scale with progressive failure (Bernander 2000; Puzrin et al. 2004; Puzrin and Germanovich 2005; Andresen and Jostad 2007; Zhang et al. 2015; Buss et al. 2019). A particular form of failure, which has been received considerable attention recently, is the retrogressive spreading failure with an uphill shear band propagation due to removal of downslope support (Quinn et al. 2011, 2012; Locat et al. 2011, 2013; Dey et al. 2016; Zhang et al. 2019b). Such phenomena occur in nature and are attributable to, for example, the erosion of riverbank and steep cut. The 1994 Sainte-Monique slide in Quebec, Canada, is a typical example initiated by riverbank erosion (Locat et al. 2015; Tran and Solowski 2019).

Initiation mechanisms and criteria for such progressive failure in sensitive soils have been well understood during the last decade (Puzrin et al. 2004; Puzrin and Germanovich 2005; Quinn et al. 2012; Zhang et al. 2015, 2017). This study seeks to numerically explore the post-failure behaviours of the Sainte-Monique slide shedding light on the kinematics of debris flow and retrogression distance which are keys for risk assessment.

The 1994 Sainte-Monique slide

The Sainte-Monique slide occurred along a brook in Quebec on 21st April 1994 (Locat et al. 2015). Figure 1a shows a cross section of the Sainte-Monique slide. The right-hand riverbank of the brook comprises the 1979 debris deposits, implying that previous events might have relocated the brook. The new brook after the 1979 event was active and gradually re-eroded the riverbed and riverbanks, with the elevation of the riverbed lowered from 26 m in 1979 to 21 m in 1992, which was considered the main triggering factor for the 1994 event.

The elevation of the embankment crest is at around 38 m prior to the failure, with the slope height from the riverbed to the crest being 16.6 m and the slope angle being 24°. The retrogression distance by the 1994 event is about 105 m from the crest of the original slope to the backscarp of the slide, and the surface elevation after the event is at 32 m in average.

CPTU data reported by Locat et al. (2015) are shown in Fig. 1a. The shear surface was determined at the elevation of 22 to 24 m. The profile of the intact material is as follows.

- Elevation 38 to 36 m (depth 0 to 2 m): surficial brown sand.
- Elevation 33 to 36 m (depth 2 m to 5 m): soft to firm silty clay with the undrained shear strength ranging from 18 to 25 kPa.
- Elevation 33 to –6 m (depth 5 to 44 m): firm to stiff, normally consolidated to slightly over-consolidated, silty clay with the undrained shear strength ranging from 25 to 130 kPa.

Locat et al. (2015) modelled the progressive failure of the Sainte-Monique slide using a program called BIFURC, and successfully obtained the evolution of shear strength reduction in the horizontal shear band and the retrogression distance. Retrogressive behaviours are invisible in their study as the embankment was modelled by a series of truss elements. Tran and Solowski (2019) investigated the retrogressive post-failure behaviours using the Material Point Method. In their work, the initial failure was introduced by an artificial steep cut, and the post-failure mechanism was found to be influenced by the uniformly oriented grid net whereby they recommended the anti-locking technique and mesh refinement to improve the issue. This study will revisit this event by using a large deformation finite element (LDFE) method, with more general initiation history and advanced remeshing techniques, aiming to comprehensively understand the retrogressive failure mechanism and kinematics behind this event. Furthermore, the controlling factors for this type of spread failure in sensitive clays will be discussed via parametric studies, which are expected to provide a view sight on potential recurrence in this region and extend the analysis to more general cases elsewhere in the world.

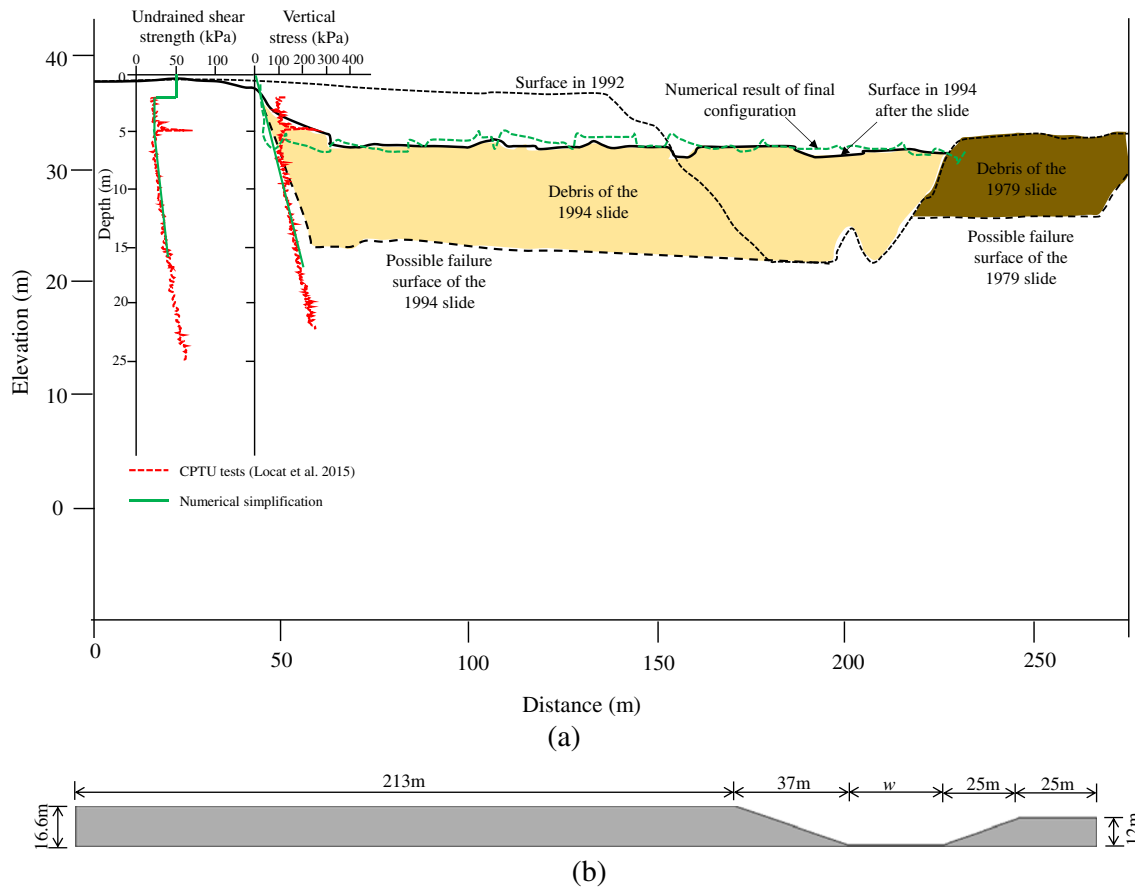


Fig. 1 a CPTU profiles and ground elevations before and after the 1994 Sainte-Monique slide (after Locat et al. 2015). b Model used in the numerical analysis

Numerical modelling

The dynamic LDFE simulation of the Sainte-Monique slide was carried out using an approach termed remeshing and interpolation technique with small strain (RITSS, Hu and Randolph 1998; Wang et al. 2010; Zhang et al. 2015). The accuracy of the RITSS method and its comparison to some other large deformation numerical methods have been discussed in Wang et al. (2015), and its applications into landslide simulations were detailed in Zhang et al. (2019a).

Geometry and soil parameters in numerical modelling

Figure 1b shows the two-dimensional plane strain model used in the numerical study. The model dimensions are determined according to the in situ topography as shown in Fig. 1a. The left-hand riverbank is 16.6 m (identical to the sliding layer thickness) in height and 237 m in length, while the right-hand embankment used to arrest the slide is 12 m in height and 25 m in length. The length of the slope at the left side of the brook is 37 m with a slope angle of 24°, while the right-hand slope is 25 m in length with a slope angle of 26°. The width of the riverbed, w , is 30 m for the base case.

Simple linear elasticity was used with Young's modulus being $E = 200\tau_p$ (where τ_p is the peak undrained shear strength) and Poisson's ratio 0.495, considering normally consolidated soils under undrained conditions. The strength reduction during shearing

is somewhat balanced by the rate effect (kinematic hardening), which can be quantified by viscoplastic models. In the present study, a power law (or the Herschel-Bulkley) type of viscoplastic model was employed. Therefore, in the plastic regime, the shear stress, τ , is given by

$$\begin{aligned} \tau &= \max \left[\tau_p + (\tau_r - \tau_p) \frac{\delta^p}{\delta_r^p}, \tau_r \right] \cdot \left(1 + \bar{K} \left| \frac{\dot{\delta}}{\dot{\delta}_{\text{ref}}} \right|^n \right) \\ &= \max \left[\tau_p + (\tau_r - \tau_p) \frac{\gamma^p}{\gamma_r^p}, \tau_r \right] \cdot \left(1 + \bar{K} \left| \frac{\dot{\gamma}}{\dot{\gamma}_{\text{ref}}} \right|^n \right) \end{aligned} \quad (1)$$

where γ^p is the accumulated plastic shear strain with $\delta^p = \gamma^p s$ being the plastic shear displacement across the weak layer, δ_r^p (γ_r^p) is the value of δ^p (γ^p) to soften the shear strength to the residual (τ_r), \bar{K} is the dimensionless viscosity coefficient, $\dot{\gamma}_{\text{ref}}$ is the reference shear strain rate with $\dot{\delta}_{\text{ref}} = \dot{\gamma}_{\text{ref}} s$ being the reference shear velocity and n is the power index. The power index n for the Canadian sensitive clays usually ranges between 0.4 and 0.6 and the dimensionless viscosity coefficient is 0.1–0.4 considering the yield stress changes between 1 and 40 kPa ($\bar{K} \approx 0.02\tau_y^{0.28}$ where τ_y is the yield stress), according to Grue (2015). In this study, the power index was set to 0.5 and the dimensionless viscosity coefficient was set to 0.2 for the base case. The shear band thickness in LDFE modelling is equal to the element size, as the shear band usually crosses one layer of meshes only. The same shear behaviour can be maintained in the

shear band by setting $\delta_r^p = \gamma_r^p s$ (where γ_r^p is the plastic shear strain at residual shear strength) regardless of the element size, s , and thus, mesh dependency due to strain softening is avoided (Zhang et al. 2015).

For simplicity, the undrained shear strength in the brown sand layer was set as constant at 50 kPa. The peak strength profile as shown in Fig. 1a was approximated by

$$\tau_p = \begin{cases} \tau_{p1} & 2m \leq h < 5m \\ \tau_{p1} + a(h-5) & h \geq 5m \end{cases} \quad (2)$$

where $\tau_{p1} = 25$ kPa is the undrained shear strength in the first, soft to firm, silty clay layer, and $a = 1.3$ kPa/m is the strength gradient along the depth h in the second, firm to stiff, silty clay layer. The sensitivity was assumed uniform over the depth and was set to 30 and the plastic shear displacement associated to the residual strength was set to 0.1 m, which is the minimum value according to Skempton (1985). The at rest lateral earth pressure coefficient was set to $K_0 = 0.5$, as the same with Tran and Solowski (2019). Other parameters for the base case are listed in Table 1 and a numerical program for parametric studies is given in Table 2.

Failure initiation

The criterion for such a type of failure is given by (Zhang and Wang 2020)

$$\frac{hK_0}{kl_u} \geq 2 + \frac{1}{S_t} \quad (3)$$

where $k = \tau_p / \sigma'_v$ (σ'_v is the effective overburden pressure) is the strength ratio at the shear surface, l_u is the characteristic length given by (Puzrin et al. 2004)

$$l_u = \sqrt{\frac{E_{ps} h \delta_r^p}{\tau_p - \tau_r}} \quad (4)$$

where E_{ps} is the modulus under plane strain conditions. For parameters given in Table 1, the critical value of k is 0.195 and hence, the critical overburden pressure is 205 kPa, which is quite

close to the in situ CPTU data as shown in Fig. 1. The effective overburden pressure on the shear surface is slightly affected by the water table. The bulk (dry) unit weight above the water table was reported to be 16 kN/m³, and the submerged unit weight is estimated as 10 kN/m³. Assuming that the river surface was 2 m below the right-hand embankment and the water table approached the river surface when the failure occurred, the effective overburden pressure on the shear surface was around 206 kPa which agrees with the analytical solution and the in situ tests. This has been further verified by a numerical modelling where an equivalent uniform unit weight was gradually increased within the ground until the failure was triggered. The critical equivalent unit weight in the numerical modelling was found to be 12.5 kN/m³ and hence, the effective overburden pressure on the shear surface (of the depth 16.6 m) is 208 kPa which is slightly above the analytical solution. To ensure slope failure, the equivalent unit weight of 13 kN/m³ (5% higher than the critical value) was used.

Numerical results

Retrogressive failure of a base case

Figure 2a and b show the contours of the current shear strength and velocity during the slide process for the base case. Three stages can be identified: failure initiation, sliding mass run-out with retrogression and sliding mass arrest with retrogression.

Failure initiation ($t \leq 2.0$ s) The shear band initiates within the bottom shear layer near the toe of the slope at $t = 2.0$ s as shown in Fig. 2. Shear strength reduction during shearing leads to the shear band propagation to adjacent intact soils, as recognised within the left-hand embankment at $t = 0.5$ s. First global failure is formed when the shear band develops from the bottom shear layer to the crest of the embankment. The shear band propagation (SBP) process occurs within 1 s, although the soil movement is still invisible.

Sliding mass run-out with retrogression (2.0 s $< t \leq 13$ s) After the first global failure at $t = 2.0$ s, the intact sliding mass breaks into several blocks and runs out along the riverbed as shown in Fig. 2. Retrogressive SBP from the main backscarp is recognised and

Table 1 Geometry and main soil parameters for the base numerical case

Parameter	Value	Unit
Average peak shear strength in sliding mass, $\bar{\tau}_{p,sm}$	33	kPa
Peak shear strength at shear surface, $\bar{\tau}_{p,ss}$	40	kPa
Soil sensitivity, S_t	30	
Plastic shear displacement to residual strength, δ_r^p	0.1	m
Young's modulus, E	$200 \tau_p^{-1}$	kPa
Poisson's ratio, ν	0.495	
At rest lateral earth pressure coefficient, K_0	0.5	
Soil unit weight, γ	13	kN/m ³
Height of embankment, H	16.6	m
Slope angle of embankment, θ	24	Degree
Width of riverbed, w	30	m

¹ τ_p is the peak shear strength in the sliding layer and varies with height, with its expression given by Eq. (4)

Table 2 Numerical program and results

Case no	$\bar{\tau}_{p,sm}$ (kPa)	S_t	δ (m)	K_0	w (m)	\bar{K}	KE (kJ) ¹	RD (m) ²
Effect of sensitivity, S_t								
C01	33.25	80	0.1	0.5	30	0.2	16.8	137
C02	33.25	30	0.1	0.5	30	0.2	11.7	106
C03	33.25	20	0.1	0.5	30	0.2	9.3	92
C04	33.25	10	0.1	0.5	30	0.2	4.7	58
Effect of average shear strength of sliding mass, $\bar{\tau}_{p,sm}$								
C05	20	30	0.1	0.5	30	0.2	16.8	138
C02	33.25	30	0.1	0.5	30	0.2	11.7	106
C06	40	30	0.1	0.5	30	0.2	9.4	88
C07	48	30	0.1	0.5	30	0.2	8.6	69
Effect of sliding displacement to the residual shear strength, δ								
C08	33.25	30	0.05	0.5	30	0.2	14.9	203
C02	33.25	30	0.1	0.5	30	0.2	11.7	106
C09	33.25	30	0.2	0.5	30	0.2	8.6	69
C10	33.25	30	0.4	0.5	30	0.2	5.2	40
Effect of dimensionless viscosity coefficient, \bar{K}								
C11	33.25	30	0.1	0.5	30	0.0	18.3	130
C02	33.25	30	0.1	0.5	30	0.2	11.7	106
C12	33.25	30	0.1	0.5	30	0.4	8.2	78
C13	33.25	30	0.1	0.5	30	0.8	5.1	64
Effect of riverbed width, w								
C14	33.25	30	0.1	0.5	10	0.2	8.4	73
C02	33.25	30	0.1	0.5	30	0.2	11.7	106
C15	33.25	30	0.1	0.5	50	0.2	12.9	138
C16	33.25	30	0.1	0.5	80	0.2	13.2	160

¹ Kinetic energy² Retrogression distance

attributed to the run-out of the frontal sliding mass. Due to dynamic motions, the sliding blocks are torn apart into more pieces and gradually separate from each other at $t=7.6$ s, which leads to extension of the sliding mass. At $t=7.6$ s, retrogressive SBP forms a complete failure surface through the riverbank leading to the second failure.

Sliding mass arrest with retrogression (13 s < t ≤ 53 s) The right-hand embankment acts as a barrier, arresting the sliding mass from $t=13$ s. The front block slows down during climbing the right-hand riverbank slope and is finally at rest at $t=19.6$ s. Thereafter, 'rear-end' collisions occur between following sliding blocks, resulting in extrusion of soil and hence further smash of soil blocks. Meanwhile, retrogressive failure is still active in the left-hand embankment and further escalates the scale of the slide. The battle between retrogression and arrest of sliding mass ends at $t=53$ s, when a stable configuration is formed. The frontal failed mass is finally deposited at the crest of the right-hand embankment, which is consistent with the site investigation.

Figure 3 plots the evolutions of the kinetic energy and maximum sliding velocity during the slide process. As expected, the sliding velocity during a retrogressive spreading failure is relatively moderate compared to a steep slope failure with the largest value less than 10 m/s in the base case. Crests and troughs of the maximum sliding velocity and kinetic energy curves occur repeatedly identifying the retrogression repeats. The kinetic energy released by the slide gradually increases to the peak at $t=10$ s when the frontal sliding block has been arrested by the right-hand embankment and generally decreases thereafter with periodical small increases by retrogressive failure. The retrogression distance recognised in the base numerical case is 107 m from the crest of the initial embankment to the final backscarp of the slide, which is very close to the in situ observation (105 m). Though the retrogression speed (nearly 2 m/s in the base case) is lower than the run-out speed of the sliding mass (up to 10 m/s), it is still very dramatic for evacuation.

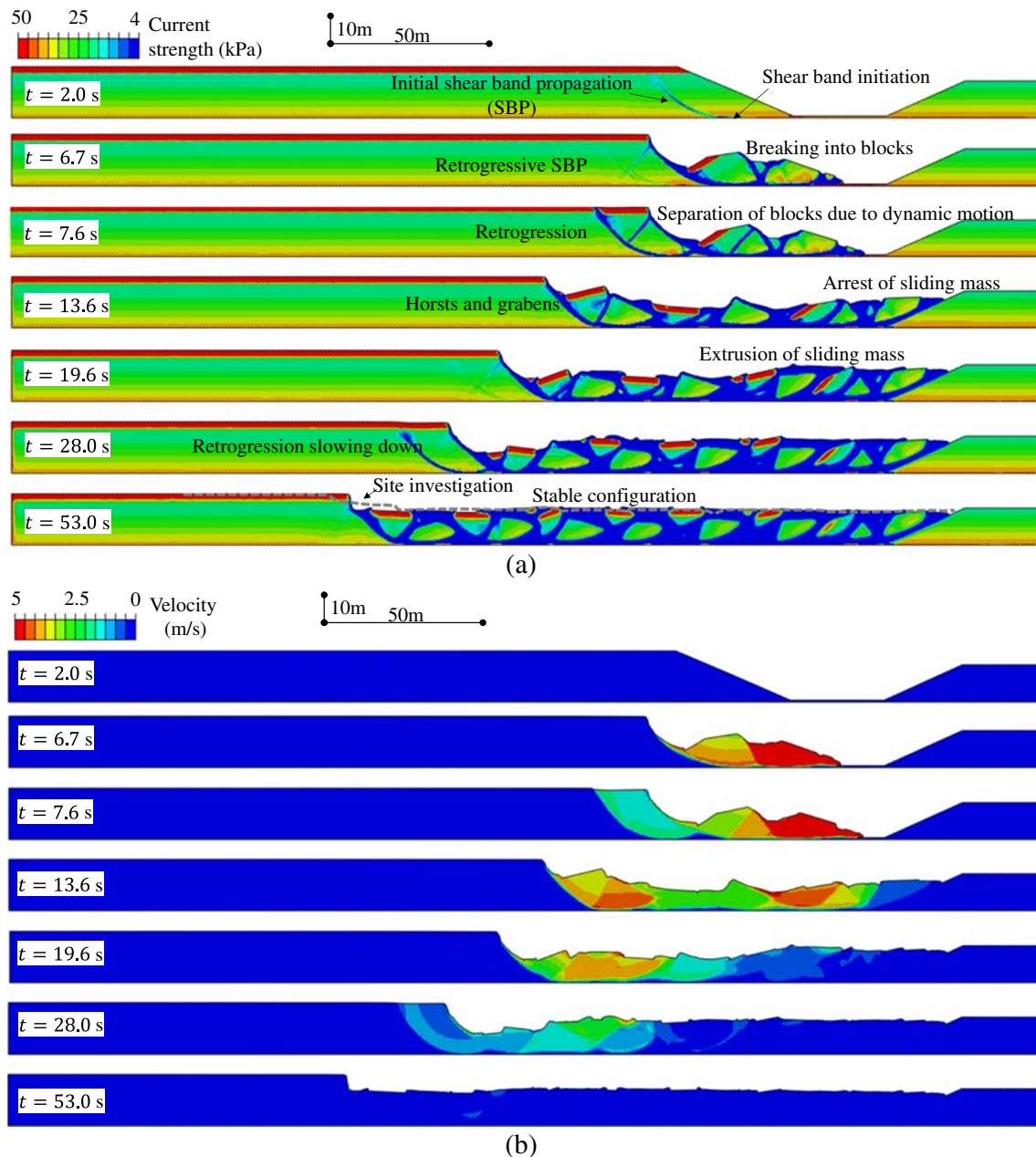


Fig. 2 Contours of **a** current shear strengths and **b** sliding velocities at different time after failure for the base case (C02 with parameters listed in Table 2)

Investigation into controlling parameters

Effect of soil sensitivity, S_t

A parametric study was conducted with S_t varying between 10, 20, 30 and 80. The residual shear strength, τ_r , of the soft clay (with constant $\tau_p = 25$ kPa) in the first layer is 2.5 kPa, 1.25 kPa, 0.83 kPa and 0.31 kPa, respectively.

Figure 4 shows contours of shear strength for at rest configurations with different values of soil sensitivity. When soil sensitivity is relatively low (i.e. $S_t = 10$), the run-out distance of the sliding mass is limited with 5 retrogression repeats. For other cases with moderate or high values of $S_t = 10, 30$ and 80, sliding masses approach the right-hand embankment with significant

retrogressive failure observed within the left-hand embankment. The elevation of the final configuration surface and retrogression distance increase with the increase of the soil sensitivity. For the case of $S_t = 80$, the sliding mass even overflows the right-hand embankment. The loss of the sliding mass potential energy depends on the residual strength of soils. The higher the sensitivity is, the smaller the potential energy can be dissipated and hence, the higher elevation the failed mass can reach.

The maximum kinetic energy and retrogression distance are summarised in Table 2. The maximum kinetic energy increases by over 3.5 times (from 4.7 to 16.8 kJ) with soil sensitivity increasing

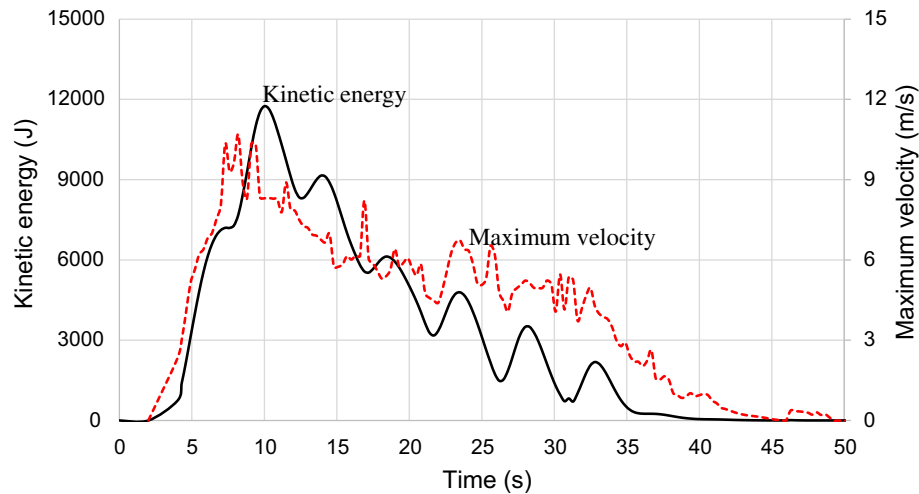


Fig. 3 Evolutions of the kinetic energy of the sliding mass and maximum sliding velocity after failure for the base case (C02 with parameters listed in Table 2)

from 10 to 80. Meanwhile, the retrogression distance increases from 58 to 137 m with increasing soil sensitivity from 10 to 80.

Effect of sliding mass shear strength, $\bar{\tau}_{p,sm}/\bar{\tau}_{p,ss}$

In order to explore the effect of the sliding mass shear strength, a parametric study was conducted with the strength ratio, $\bar{\tau}_{p,sm}/\bar{\tau}_{p,ss}$, varying between 0.5, 0.8, 1.0 and 1.2. The value of $\bar{\tau}_{p,ss}$ was fixed at 40 kPa among the four cases. The value of $\bar{\tau}_{p,sm}$ linearly changes from 0.1 kPa at the surface to 40 kPa at the shear surface for the case of $\bar{\tau}_{p,sm}/\bar{\tau}_{p,ss} = 0.5$, while is constant through the sliding mass at $\bar{\tau}_{p,sm} = 40$ kPa and 48 kPa for the cases of $\bar{\tau}_{p,sm}/\bar{\tau}_{p,ss} = 1.0$ and 1.2, respectively. A preliminary simulation shows that for the strength ratio $\bar{\tau}_{p,sm}/\bar{\tau}_{p,ss} = 1.3$ ($\bar{\tau}_{p,sm} = 52$ kPa), shear band is localised near the toe of the slope without global slope failure.

Figure 5 shows contours of shear strength for at rest configurations with respect to the effect of the sliding mass strength. Horsts and grabens are more significant in cases of high values of $\bar{\tau}_{p,sm}/\bar{\tau}_{p,ss}$ (1.0 and 1.2), as strong sliding mass are difficult to tear apart during the slide process. For the case of $\bar{\tau}_{p,sm}/\bar{\tau}_{p,ss} = 0.5$, soils are too weak to form horst and graben, and the sliding failure is more like a ‘debris flow’. As listed in Table 2, the strength ratio $\bar{\tau}_{p,sm}/\bar{\tau}_{p,ss}$ has limited effect on the maximum kinetic energy of the

sliding mass and retrogression distance. The retrogression distance increases from 69 to 138 m with decreasing the strength ratio $\bar{\tau}_{p,sm}/\bar{\tau}_{p,ss}$ from 1.2 to 0.5.

Effect of shear displacement associated to the residual strength, δ_r^p/s

The plastic shear displacement at the residual shear strength, δ_r^p , governs the softening rate (or soil brittleness) and is hence expected to influence the retrogressive failure. The effect with the normalised plastic shear displacement at the residual shear strength, δ_r^p/s , was investigated, by varying its value between 0.125, 0.25, 0.5 and 1.0 (accordingly, $\delta_r^p = 0.05$ m, 0.1 m, 0.2 m and 0.4 m respectively).

Figure 6 shows contours of shear strength for at rest configurations with different values of δ_r^p/s . With decreasing δ_r^p/s , the elevation of the final configuration surface rises, and the horsts and grabens become obvious. This implies retrogressive failure is more likely to occur in brittle materials. Kinetic energies occupied by the sliding mass in brittle clays are larger than those in ductile clays, and retrogression distances in brittle clays are farther. For example, the retrogression distance is 40 m in the case of $\delta_r^p/s = 1.0$ and increases to 203 m in the case of $\delta_r^p/s = 0.125$, as listed in Table 2.

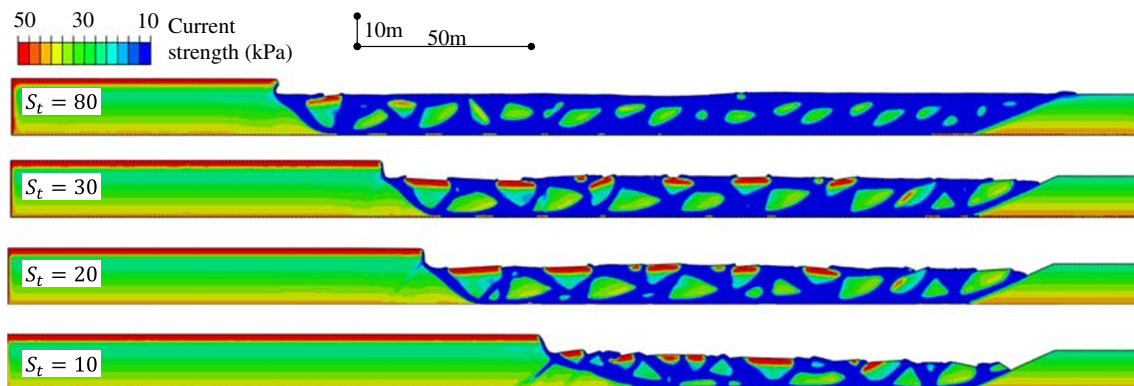


Fig. 4 Shear strength contours and stratigraphy of sliding mass deposits with respect to the effect of the soil sensitivity S_t

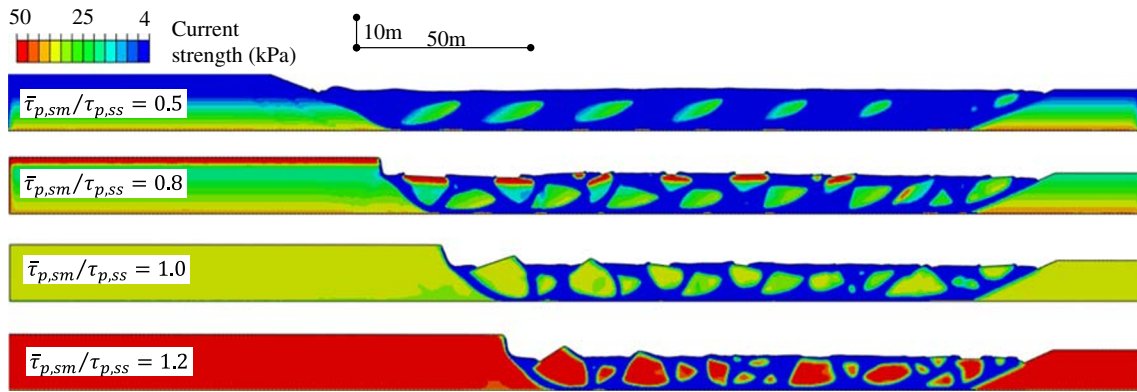


Fig. 5 Shear strength contours and stratigraphy of sliding mass deposits with respect to the effect of the average shear strength of the sliding mass, $\bar{\tau}_{p,sm}$

Effect of dimensionless viscosity coefficient, \bar{K}

Saturated clay exhibits increasing shear strength with increasing shear strain rate, and the shear strength and rheology properties may span different orders of magnitude during shearing. A parametric study with respect to the effect of the dimensionless viscosity effect \bar{K} was conducted with its value varying between 0.0, 0.2, 0.4 and 0.8.

Figure 7 shows shear strength contours at the final state for different cases. For the case without rate effect ($\bar{K} = 0.0$), the retrogressive failure is the most significant and the sliding mass is the least intact due to the dynamic collisions between soil blocks. For the case of viscosity, the kinetic energy was partly dissipated through the damping leading to less significant dynamic effect and hence more obvious horsts and grabens. The retrogression distance decreases from 130 to 64 m as the value of \bar{K} increases from 0.0 to 0.8. Correspondingly, the maximum kinetic energy decreases from 18.3 to 5.1 kJ.

Effect of riverbed width, w/H

The width of the riverbed might be different at different sections of the brook and change with the river detour (caused by, e.g., slide). It determines the distance of a barrier (here the right-hand embankment) that may arrest the sliding mass and is hence expected to have an impact on retrogressive failure. A parametric study was conducted with the riverbed width various between 10 m, 30 m,

50 m and 100 m (i.e. $w/H = 0.6, 1.8, 3$ and 6 where $H = 16.6$ m is the embankment height).

Figure 8 shows contours of shear strength at final stages with respect to the effect of the normalised riverbed width w/H . With increasing the riverbed width (or the distance from the barrier to the slope), the sliding mass is disassembled more significantly. The maximum kinetic energy occupied by the sliding mass increases from 8.4 to 12.9 kJ while the retrogression distance increases from 73 to 138 m, when w/H increases from 0.6 to 3.0. However, when further increasing the normalised riverbed width from 3.0 to 6.0, the maximum kinetic energy and the regression distance are increased by only 0.3 kJ and 22 m, respectively.

Discussions

As indicated in Fig. 2, retrogressive spreading failure in sensitive clays is formed by two competitive types of SBP: nearly horizontal SBP along the shear surface and rotational SBP in the overlying embankment. Such failure is particularly common with existence of weak layers, within which sediments have a lower undrained shear strength relative to the effective normal stress than for adjacent layers. Due to stratification arising from natural sedimentation, weak layers are usually observed or assumed parallel to the slope surface. Therefore, failure is usually initiated within the weak

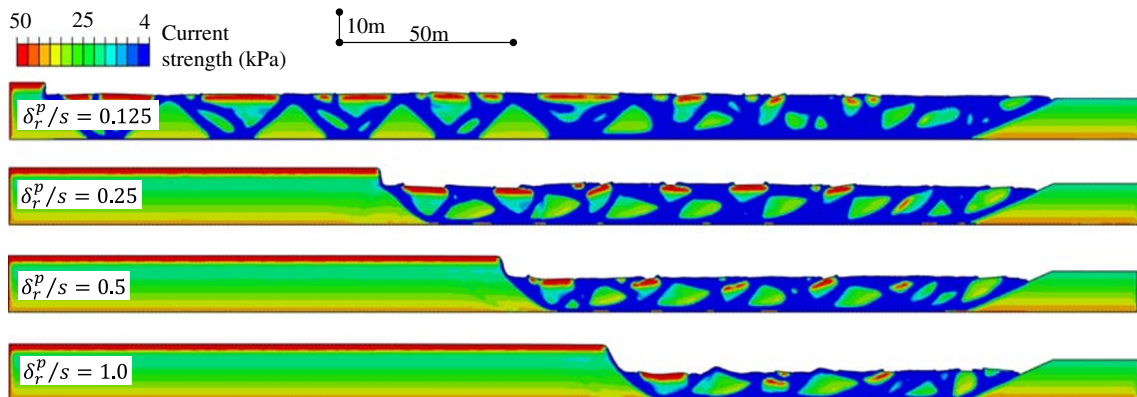


Fig. 6 Shear strength contours and stratigraphy of sliding mass deposits with respect to the effect of the plastic shear displacement to the residual strength, δ_r^p

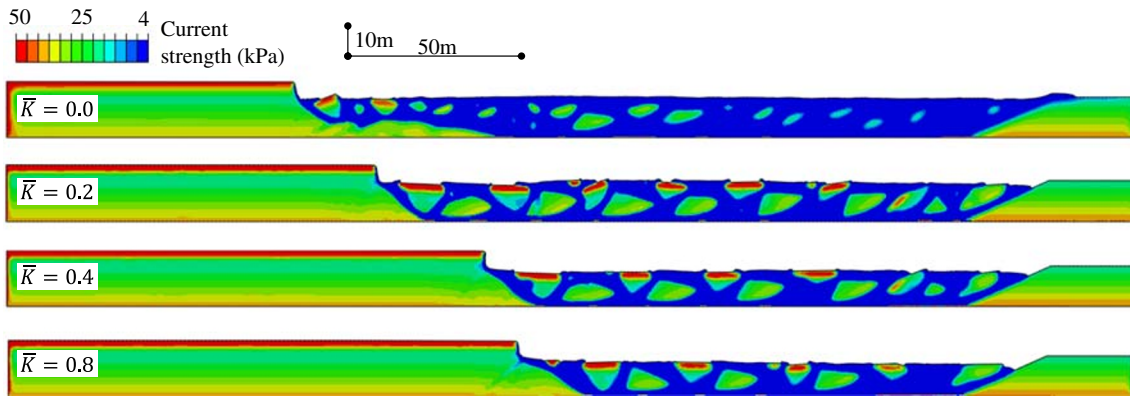


Fig. 7 Shear strength contours and stratigraphy of sliding mass deposits with respect to the effect of the dimensionless viscosity coefficient, \bar{K}

layer at the toe of a slope, followed by horizontal SBP along the weak layer. SBP process results in the decrease of the lateral earth pressure and finally active failure within the embankment. Formation of a complete shear band in the embankment leads to run-out of sliding mass and restricts the horizontal SBP in the weak layer, which will be reactive with the lowering of the sliding mass. Such a competitive relationship between horizontal and rotational SBP repeats and forms retrogressive failure. The scale of retrogressive failure can be raised by either increasing successive failure repeats or horizontal SBP distance along the weak layer.

According to the above parametric studies, retrogressive failure is very sensitive to parameters controlling strain softening and rate effects such as S_b , δ_r^p and \bar{K} . Increase of S_t and decrease of δ_r^p and \bar{K} can impair soil strength during shearing and hence facilitate retrogressive failure by means of increasing successive failure repeats. This explains frequent retrogressive failure in Norway and Canada where highly sensitive or quick clays are abundant.

Existence of a barrier considerably restricts the retrogressive failure when it is sufficiently close to the failed slope. However, when the distance from the barrier to the slope succeeds a critical value (30 m in the 1994 SM case), the barrier may still arrest the sliding mass but is failed to effectively restrict the retrogressive failure as shown in Fig. 8. Therefore, a careful design is necessary for setting an efficient downstream barrier to mitigate a potential retrogressive failure.

The dynamic motion of the sliding mass is affected by the soil viscosity particularly during the initiation stage. The failure initiation is instant for the case without rate effect where the kinetic energy is increased rapidly. For the case of heavy viscosity ($\bar{K} = 0.8$), however, the kinetic energy remains almost zero for nearly 100 s showing a creeping failure initiation. A longer initiation period is expected with heavier viscosity or lower equivalent unit weight (such that the slope is closer to the critical condition). The initiation time for the SM slide is uncertain from published resources, while it lasted for over 3 h from the little instability warning to the first major failure for the Saint Jean Vianney slide occurred in 1971 in Quebec Canada (Tavenas et al. 1971). The effect of soil rheology on pre-failure duration has also been revealed by Zhang et al. (2019a), where the initiation time can be increased by two orders of magnitude with the viscosity coefficient increased by four times.

The retrogressive failure duration is governed by the scale of the slide (retrogression distance) in addition to the dynamic motion related to the viscous effect. From the numerical modelling, it took about 150 s to complete a series of retrogressive failure with the retrogression distance of 64 m for the case of $\bar{K} = 0.8$ while about 50 s for the case of $\bar{K} = 0.2$ with retrogression distance of 106 m. As a comparison, a series of retrogressive failure with retrogression distance of 150 m took about 300 s for the Saint Jean Vianney slide (Tavenas et al. 1971) and the most recent spread failure in Alta Norway on 3 June 2020 took about a couple of minutes to complete the second phase of the failure (Petley 2020).

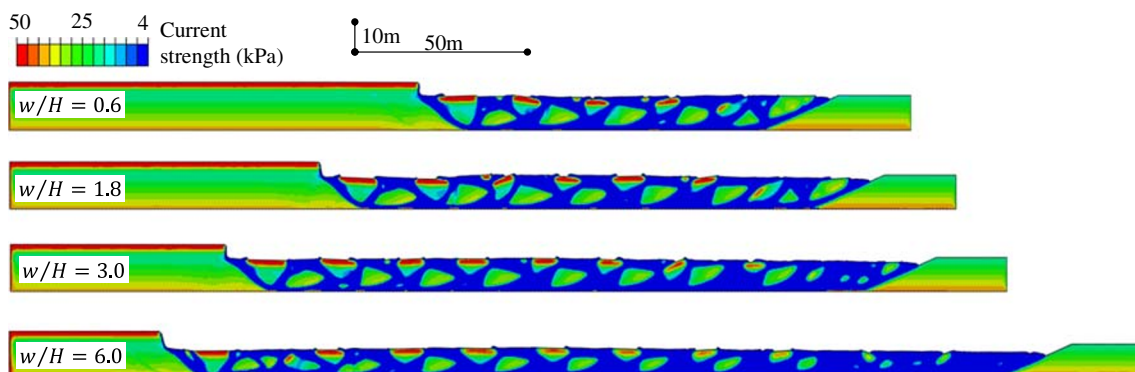


Fig. 8 Shear strength contours and stratigraphy of sliding mass deposits with respect to the effect of the riverbed width w

Conclusions

The paper has revisited and simulated the 1994 Sainte-Monique slide in Quebec by using a large deformation finite element method termed as ‘remeshing and interpolation technique with small strain’ (RITSS). Focus has been on the factors determining the post-failure kinematics and retrogression distance through numerical investigations.

Key features in retrogressive failure, such as the formation of grabens and horsts and retrogressive shear band propagation (SBP), have been successfully reproduced in the numerical analysis. The retrogression distance and at rest configuration of the sliding mass are comparable to site investigations. Shear band is initiated near the toe of the slope due to riverbed erosions, followed by SBP leading to global failure with sliding mass running out and retrogression into intact upstream embankment. The sliding mass is arrested by the other side riverbank with soil blocks subjected to ‘rear-end’ collisions and smashed into debris.

The kinetic energy and retrogression distance of a slide are very sensitive to strain softening-related parameters such as the soil sensitivity S_r and plastic shear displacement at the residual shear strength δ_r^p . Existence of a barrier considerably restricts the retrogressive failure when it is close enough to the failed slope. However, when the distance from the barrier to the slope succeeds a critical value, the barrier may be failed to restrict the retrogressive failure. The failure initiation and retrogression duration are also greatly affected by the viscous effect of soils.

Funding

Open access funding provided by Swiss Federal Institute of Technology Zurich. This research is supported by the Key Science and Technology Plan of PowerChina Huadong Engineering Corporation (KY2018-ZD-01) and the National Natural Science Foundation of China (through the grants of Nos. U1806230 and 41772294). The second author also thanks the support from Prof. Alexander Puzrin (the Chair of Geotechnical Engineering - Geomechanics, ETH Zurich) and the Centre for Offshore Foundation Systems (COFS, UWA) through the Fugro Chair in Geotechnics.

Open Access This article is licensed under a Creative Commons Attribution 4.0 International License, which permits use, sharing, adaptation, distribution and reproduction in any medium or format, as long as you give appropriate credit to the original author(s) and the source, provide a link to the Creative Commons licence, and indicate if changes were made. The images or other third party material in this article are included in the article's Creative Commons licence, unless indicated otherwise in a credit line to the material. If material is not included in the article's Creative Commons licence and your intended use is not permitted by statutory regulation or exceeds the permitted use, you will need to obtain permission directly from the copyright holder. To view a copy of this licence, visit <http://creativecommons.org/licenses/by/4.0/>.

References

Andresen L, Jostad HP (2007) Numerical modelling of failure mechanisms in sensitive soft clay – application to offshore geohazard. Offshore Technology Conference, Houston, Texas, USA, 30 April–3 May, No. OTC 18650

- Bernander S (2000) Progressive landslides in long natural slopes, formation, potential extension and configuration of finished slides in strain-softening soil. Licentiate thesis, Luleå University of Technology, Luleå, Sweden
- Buss C, Friedli B, Puzrin AM (2019) Kinematic energy balance approach to submarine landslide evolution. *Can Geotech J* 56(9):1351–1365
- Crawford CB (1968) Quick clays of eastern Canada. *Eng Geol* 2(4):239–265
- Dey R, Hawlader BC, Phillips R, Soga K (2016) Modeling of large deformation behaviour of marine sensitive clays and its application to submarine slope stability analysis. *Can Geotech J* 53(7):1138–1155
- Gregersen O, Loken T (1979) The quick-clay slide at Baastad, Norway, 1974. *Eng Geol* 14(2–3):183–196
- Grue RH (2015) Rheology parameters of Norwegian sensitive clays, focusing on the Herschel-Bulkley model. Master thesis. Trondheim: Institute of Civil and Transport Engineering, NTNU
- Gylland A, Long M, Emdal A, Sandven R (2013) Characterisation and engineering properties of Tiller clay. *Eng Geol* 164:86–100
- Hu Y, Randolph MF (1998) A practical numerical approach for large deformation problem in soil. *Int J Numer Anal Methods Geomech* 22(5):327–350
- Kerr PF, Drew IM (1968) Quick-clay slides in the USA. *Eng Geol* 2(4):215–238
- Locat A, Leroueil S, Bernander S, Demers D, Jostad HP, Ouehb L (2011) Progressive failure in eastern Canadian and Scandinavian sensitive clays. *Can Geotech J* 48(11):1696–1712
- Locat A, Jostad HP, Leroueil S (2013) Numerical modelling of progressive and its implications for spreads in sensitive clays. *Can Geotech J* 50(9):961–978
- Locat A, Leroueil S, Fortin A, Demers D, Jostad HP (2015) The 1994 landslide at Sainte-Monique, Quebec: geotechnical investigation and application of progressive failure analysis. *Can Geotech J* 52(4):490–504
- Lundstrom K, Larsson R, Dahlin T (2009) Mapping of quick clay formations using geotechnical and geophysical methods. *Landslides* 6:1–15
- Petley D (2020) Alta: a truly remarkable video of a quick clay landslide in Norway. AGU Blogosphere. <https://blogs.agu.org/landslideblog/2020/06/04/alta-quick-clay-landslide-1/>. Accessed 4 June 2020.
- Puzrin AM, Germanovich LN (2005) The growth of shear bands in the catastrophic failure of soils. *Proc R Soc Ser A Math Phys Engng Sci* 461(2056):1199–1228
- Puzrin AM, Germanovich LN, Kim S (2004) Catastrophic failure of submerged slopes in normally consolidated sediments. *Géotechnique* 54(10):631–643
- Quinn PE, Diederichs MS, Rowe RK, Hutchinson DJ (2011) A new model for large landslides in sensitive clay using a fracture mechanics approach. *Can Geotech J* 48(8):1151–1162
- Quinn PE, Diederichs MS, Rowe RK, Hutchinson DJ (2012) Development of progressive failure in sensitive clay slopes. *Can Geotech J* 49(7):782–795
- Skempton AW (1964) Long-term stability of clay slopes. *Géotechnique* 14(2):77–102
- Skempton AW (1985) Residual strength of clays in landslides, folded strata and the laboratory. *Géotechnique* 35(1):3–18
- Solberg IL, Hansen L, Rokoengen K (2008) Large, prehistoric clay slides revealed in road excavations in Buvika, mid-Norway. *Landslides* 5:291–304
- Tavenas F, Chagnon JY, Rochelle PL (1971) The Saint-Jean-Vianney landslide: observations and eyewitness accounts. *Can Geotech J* 8(3):463–478
- Tran QA, Solowski W (2019) Generalized Interpolation Material Point Method modelling of large deformation problems including strain-rate effects – application to penetration and progressive failure problems. *Comput Geotech* 106:249–265
- Wang D, Bienen B, Nazem M, Tian Y, Zheng J, Pucker T, Randolph M (2015) Large deformation finite element analyses in geotechnical engineering. *Comput Geotech* 65:104–114
- Wang D, Hu Y, Randolph MF (2010) Three-dimensional large deformation finite element analysis of plate anchors in uniform clay. *J Geotech Geoenviron* 136(2):355–365
- Zhang W, Randolph MF, Puzrin AM, Wang D (2019a) Transition from shear band propagation to global slab failure in submarine landslides. *Can Geotech J* 56(4):554–569
- Zhang W, Wang D (2020) Stability analysis of cut slope with shear band propagation along a weak layer. *Comput Geotech* 125:103676. <https://doi.org/10.1016/j.compgeo.2020.103676>
- Zhang W, Wang D, Randolph MF, Puzrin AM (2015) Catastrophic failure in planar landslides with a fully softened weak zone. *Géotechnique* 65(9):755–769
- Zhang W, Wang D, Randolph MF, Puzrin AM (2017) From progressive to catastrophic failure in submarine landslides with curvilinear slope geometries. *Géotechnique* 67(12):1104–1119
- Zhang X, Oñate E, Torres SAG, Bleyer J, Krabbenhoft K (2019b) A unified Lagrangian formulation for solid and fluid dynamics and its possibility for modelling submarine landslides and their consequences. *Comput Methods Appl Mech Eng* 343:314–338

Z. Shan

PowerChina Huadong Engineering Corporation Limited,
Hangzhou, China
e-mail: shan_zg@ecidi.com

W. Zhang

Institute for Geotechnical Engineering, Institute for Geotechnical Engineering,
ETH Zurich,
Zurich, Switzerland

W. Zhang 

Oceans Graduate School,
The University of Western Australia,
Perth, Australia
Email: wangcheng.zhang@uwa.edu.au

D. Wang

College of Environmental Science and Engineering,
Ocean University of China,
Qingdao, China
e-mail: dongwang@ouc.edu.cn

D. Wang

Qingdao National Laboratory for Marine Science and Technology,
Qingdao, China

L. Wang

Ocean College,
Zhejiang University,
Hangzhou, China
e-mail: wanglz@zju.edu.cn